PAPER • OPEN ACCESS

Slowing of acoustic waves in electrorheological and string-fluid complex plasmas

To cite this article: M Schwabe *et al* 2020 *New J. Phys.* **22** 083079

View the article online for updates and enhancements.

New Journal of Physics

The open access journal at the forefront of physics

Deutsche Physikalische Gesellschaft **DPG**

IOP Institute of Physics

Published in partnership with: Deutsche Physikalische Gesellschaft and the Institute of Physics

PAPER

Slowing of acoustic waves in electrorheological and string-fluid complex plasmas

M Schwabe[1,7] , S A Khrapak[1] , S K Zhdanov[1], M Y Pustylnik[1], C Räth[1], M Fink[1],
M Kretschmer[2], A M Lipaev[3,4] , V I Molotkov[3,6] , A S Schmitz[2], M H Thoma[2],
A D Usachev[3], A V Zobnin[3], G I Padalka[5], V E Fortov[3], O F Petrov[3] and H M Thomas[1]

[1] Institut für Materialphysik im Weltraum, Deutsches Zentrum für Luft- und Raumfahrt (DLR), 82234 Weßling, Germany
[2] I. Physikalisches Institut, Justus-Liebig-Universität Gießen, 35392 Gießen, Germany
[3] Joint Institute of High Temperatures, Russian Academy of Sciences, 125412 Moscow, Russia
[4] Moscow Institute of Physics and Technology (MIPT), 9 Institutsky per., Dolgoprudny, 141701, Russia
[5] Gagarin Research and Test Cosmonaut Training Center, 141160 Star City, Moscow Region, Russia
[6] Deceased in 2019.
[7] Author to whom any correspondence should be addressed.

E-mail: mierk.schwabe@dlr.de

Abstract

The PK-4 laboratory consists of a direct current plasma tube into which microparticles are injected, forming a complex plasma. The microparticles acquire many electrons from the ambient plasma and are thus highly charged and interact with each other. If ion streams are present, wakes form downstream of the microparticles, which lead to an attractive term in the potential between the microparticles, triggering the appearance of microparticle strings and modifying the complex plasma into an electrorheological form. Here we report on a set of experiments on compressional waves in such a string fluid in the PK-4 laboratory during a parabolic flight and on board the International Space Station. We find a slowing of acoustic waves and hypothesize that the additional attractive interaction term leads to slower wave speeds than in complex plasmas with purely repulsive potentials. We test this hypothesis with simulations, and compare with theory.

1. Introduction

Electrorheological (ER) and magnetorheological (MR) fluids change their rheology drastically when electric resp. magnetic fields are applied [1–4]. They typically consist of microparticles suspended in a non-conducting carrier fluid. When an external field is applied, dipoles are induced, and the particles arrange in strongly coupled chains ('strings'), sheets, or compressed crystalline structures. This leads to a reversible increase in effective viscosity. ER and MR fluids have a significant potential for applications, for instance in vibration control in smart materials [5], bio-medicine [6], and sound propagation [7]. ER fluids transmit sound better (i.e., with less loss) when a higher voltage is applied [8], and the velocity of sound in ER fluids increases with electric field strength when the longitudinal wave propagates in parallel with the electric field [9–11]. However, in an MR slurry of iron particles in glycerine, two longitudinal modes of sound have been identified, with the speed of sound depending on the strength of the applied magnetic field [7, 12]. A 'second' sound mode can also occur as a wave of density of collective quasiparticle excitations [13].

Here, we report the first experimental study on the propagation of dust compressional waves in an ER complex plasma. Complex plasmas are low temperature plasmas that contain micrometer-sized particles (microparticles/'dust') in addition to ions, electrons, and neutral particles. Typically, a laser plane illuminates the microparticles, and a camera records their positions, which allows experimenters to follow the motion of individual microparticles from frame to frame.

The plasma ions and electrons charge the microparticles highly negatively, so that the microparticles strongly interact with each other. The microparticles then can serve as 'proxy atoms' for conventional systems, and the complex plasma forms a model system. Complex plasmas display a wealth of fluid phenomena, for instance, they form waves [14–17], lanes in crossing flows [18], turbulence [19–21], flow structures behind obstacles [22–24], and rogue waves [25].

Gravity pulls the microparticles toward the bottom sheath of the plasma, where a strong electric field levitates them. This electric field also leads to inhomogeneities and strong ion flows, which in turn cause wakes [26–28], subsequent particle chains [29–35] and additional instabilities in the microparticle cloud [36]. A strong vertical temperature gradient can compensate for gravity [37], but associated thermal creep forces can cause instabilities [38]. Therefore, it is desirable to perform experiments in microgravity, where the microparticles are levitated in the bulk of the plasma.

One possibility to achieve weightless conditions is to perform a parabolic flight, in which the experiment is installed on board an aircraft that follows a flight trajectory that compensates for gravity for approximately 22 s with an accuracy of better than $\pm 0.05 g$, with g being the acceleration of gravity on Earth. On board the International Space Station (ISS), gravity is compensated by the station's orbital motion, which provides very favorable weightless conditions [39–41]. This is why we study complex plasmas in a complex plasma laboratory on board the ISS, PK-4 [42], which follows its predecessors PKE-Nefedov [43] and PK-3 Plus [44].

This manuscript is organized as follows: In section 2 we introduce the experimental setup and conditions. In section 3 we present the experimental findings of four experimental runs, which we then discuss and link with theory in section 4. Finally, we conclude in section 5 and give computational details in appendices A and B.
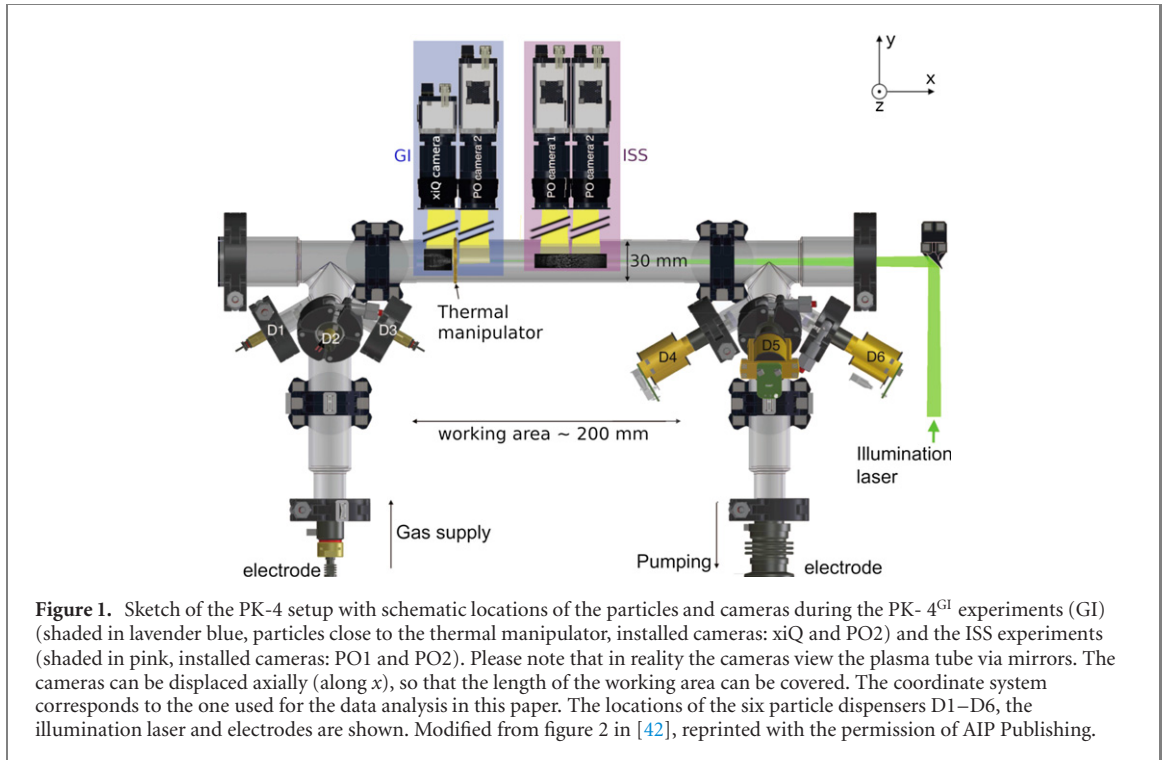
2. Experimental conditions

2.1. Experimental setup

The heart of the PK-4 laboratory consists of a direct current (DC) plasma tube with 3 cm diameter and a working area of 20 cm length, see figure 1. A discharge between an active and a passive electrode ionizes the gas in the tube, forming a plasma. Particle dispensers inject microparticles into the system, which stream through the tube and can be trapped in the working area visible by the cameras. This can be achieved via polarity switching: when an electric field is applied to the complex plasma that is alternating with a frequency much larger than the microparticle plasma frequency (10–100 Hz) and much smaller than the ion plasma frequency (about 10 MHz) [45], the microparticles experience an averaged electric field depending on the duty cycle of the polarity switching. If the duty cycle is selected carefully, small residual forces such as that from a gas flow can be compensated, trapping the microparticles in the tube. The microparticle flow can also be stopped by a thermal manipulator which consists of a heater ring that is mounted on the outer surface of the plasma tube. It can produce an axial temperature gradient that causes thermophoresis [37] and thermal creep [38, 46–49]. A laser, shown in green in figure 1, illuminates a slice of the three-dimensional (3D) particle cloud. Several manipulation devices are able to shape the microparticle flow.

In this paper we report on experiments performed in two models of the setup. The European-Russian *ISS laboratory PK-4* [42] is mounted in the Columbus module of the ISS. In this setup, two particle observation (PO) cameras, shown in figure 1 in the pink shaded region, record the images of the microparticles. The cameras can be moved along the *x* direction, in parallel to the tube axis, with a translation stage. The fields of view of these cameras overlap by approximately 1.4 mm, which makes it possible to combine the two images into one by finding the positions of particles in the overlap region in the images from both cameras and calculating the best fitting affine transformation between them [50]. The combined field of view (FOV) is about 44×17 mm^2 at a spatial resolution of 14.2 μm/pixel. The waist of the illumination laser lies approximately in the middle of the combined FOV. A plasma glow observation system records overview images showing a spectrum-integrated plasma image including the light of the lasers resp. images in which only the wavelengths of two spectral lines of neon are shown.

The *parabolic flight setup* PK-4^{GI} [51] is mounted in a rack located at the Justus-Liebig University in Gießen, Germany and is regularly flown on parabolic flights. Compared with the ISS laboratory, the PO camera 1 was replaced by a CMOS camera (xiQ) with higher resolution (4 MPixel at a resolution of 11.8 μm/pixel and a frame rate of 90 fps) (indicated in figure 1 with the lavender blue shaded region), and other small modifications were made. The main features of the two laboratories are identical.

Figure 1. Sketch of the PK- 4 setup with schematic locations of the particles and cameras during the PK- 4^{GI} experiments (GI) (shaded in lavender blue, particles close to the thermal manipulator, installed cameras: xiQ and PO2) and the ISS experiments (shaded in pink, installed cameras: PO1 and PO2). Please note that in reality the cameras view the plasma tube via mirrors. The cameras can be displaced axially (along *x*), so that the length of the working area can be covered. The coordinate system corresponds to the one used for the data analysis in this paper. The locations of the six particle dispensers D1–D6, the illumination laser and electrodes are shown. Modified from figure 2 in [42], reprinted with the permission of AIP Publishing.

2.2. Charges and potentials

Once particles are injected into the plasma, they quickly attain high negative charges. Recently, Antonova *et al* [52] measured the microparticle charge in the ISS PK-4 laboratory by considering the force balance acting on individual microparticles. Irrespective of gas pressure, for neon plasmas they measured a reduced charge of

$$z = \frac{Z_d e^2}{4\pi\epsilon_0 k_B T_e r_d} \approx 0.3, \tag{1}$$

where $Q_d = Z_d e$ and r_d are the microparticle charge and radius, respectively, Z_d is the microparticle charge number, e denotes the charge of an electron, ϵ_0 is the vacuum permittivity, k_B is Boltzmann's constant, and T_e is the electron temperature. This experimentally measured reduced charge is smaller than previously theoretically estimated [53]. Nevertheless, we shall use it in the following, since these dedicated experiments had a high precision and are not inconsistent with previously reported experimental measurements [54, 55].

As mentioned above, in both the ISS and GI setups, particles can either be trapped by applying a temperature gradient with the thermal manipulator, or by polarity switching. During polarity switching, the frequency of the electric field is such that the ions are light enough to follow the alternating electric force. This leads to a symmetric attractive potential between the microparticles caused by positive ion wakes downstream of the microparticles. The microparticles then interact via both the typical Yukawa potential

$$\phi_Y = \frac{Q_d^2}{4\pi\epsilon_0 r} \exp\left(-\frac{r}{\lambda_D}\right) \tag{2}$$

and an interaction between the charge of the microparticle and the quadrupole part of the wake by another particle [56]

$$\phi_D = -0.43 \frac{Q_d^2}{4\pi\epsilon_0 r} \frac{M_{th}^2 \lambda_D^2}{r^2} (3\cos^2\theta - 1), \tag{3}$$

with the screening length λ_D, thermal ion Mach number $M_{th} = \sqrt{\langle u_i^2 \rangle / v_T^2}$—the average squared ion velocity u_i normalized by the thermal ion velocity v_T (which is equal to that of the neutrals)—and θ the angle between the accelerating electric field and the vector connecting two interacting microparticles, **r**. Since the charge-quadrupole interaction, equation (3), is equivalent to the interaction between two dipoles, we will follow [56] and call this the 'dipole' term.

The complex plasma thus forms an ER plasma, named in analogy to ER fluids [56, 57] due to the comparable dipole interactions. The effective attraction caused by the wakes often leads to the formation of

microparticle strings [58–60]. The arrangement of the axial strings probably also depends on the interaction with microparticles in neighboring chains [61].

Microparticle strings can form in complex plasmas whenever electric fields and associated ion flows become anisotropic. For the case of an oscillating electric field and bipolar wakes, the attractive part of the interaction potential is given by equation (3). In the DC case unipolar wakes form, but strings can still appear [36, 62–64]. In this case, the interparticle interactions become non-reciprocal. Therefore, we do not consider this situation in the following theory and simulation. Nevertheless, an effect on the wave velocity is observed even for strings formed due to unipolar wakes, as will be shown below.

2.3. Waves

Dust acoustic/dust density waves are longitudinal waves in the microparticle fluid [15]. They can occur spontaneously due to an ion-microparticle streaming instability [65–67] when the gas damping is low enough, and the microparticle density and the local electric field accelerating the ions are high enough [68, 69]. An approximation for the critical electric field for wave excitation is [23]

$$E \gtrsim E_{\mathrm{cr}} = \frac{\gamma_{\mathrm{Ep}}}{c_{\mathrm{DA}}} \frac{k_{\mathrm{B}} T_{\mathrm{i}}}{e}, \tag{4}$$

where γ_{Ep} is the coefficient determining the strength of the Epstein damping of the microparticle motion by the neutral gas [70], and the dust acoustic velocity c_{DA} is given by [71, 72]

$$c_{\mathrm{DA}} = \sqrt{\frac{Z_{\mathrm{d}}^2 n_{\mathrm{d}} k_{\mathrm{B}} T_{\mathrm{i}}}{m_{\mathrm{d}} n_{\mathrm{i}}}}, \tag{5}$$

where m_{d} and n_{d} stand for the microparticle mass and equilibrium density, respectively, and T_{i} and n_{i} for the ion temperature and density.

The combination of collisional and ion drift effects would modify the conventional dust acoustic velocity, as discussed in [17, 69, 73, 74]. In the considered parameter regime these effects would enhance the DA velocity by up to a factor of two. Since this contradicts experimental observations, other mechanisms should determine the physics involved, and we do not consider this modification in the following.

Expression (5) assumes no correlations between particle positions and is applicable to the weakly coupled gaseous regime. In the strongly coupled regime correlations are important, and they can be taken into account, for instance, using the fluid plasma description, supplemented by an appropriate equation of state for the particle component [75, 76]. Recently, a simple practical approach to evaluate sound velocities in strongly coupled complex plasmas in one-, two-, and three spatial dimensions has been proposed [77]. In this approach the sound velocities are expressed using the sound velocity scale

$$c_0 = \sqrt{\frac{Q_d^2}{4\pi\epsilon_0 \Delta m_d}}, \tag{6}$$

where $\Delta = n_d^{-1/\mathcal{D}}$ is the characteristic interparticle separation, with the microparticle density n_{d} and the dimensionality $\mathcal{D}$. The sound velocity is expressed as the product of this velocity scale c_0 and a screening function $f(\kappa)$, which depends on the screening parameter $\kappa = \Delta/\lambda_{\mathrm{D}}$, that is $c_{\mathrm{s}} = c_0 f(\kappa)$. The exact shape of $f(\kappa)$ depends on the dimensionality and is given in [77]. At weak screening ($\kappa \lesssim 3$), the sound velocities in different spatial dimensions are well separated and their amplitude increases with dimensionality. For stronger screening ($\kappa \gtrsim 3$), the sound velocities in different dimensions all approach the same asymptote corresponding to the one-dimensional (1D) lattice with nearest-neighbor interactions. This is a general result for sufficiently steep interactions, which can considerably simplify the evaluation of the sound velocity in related systems.

Compressional waves in an ER plasma can also be induced by a charge-gradient instability, as was recently shown by Yaroshenko [78]: charge gradients along the direction of string formation can be induced by the modified charging due to ion wakes. This then can lead to an instability of the strings and subsequent propagation of waves along the direction of the charge gradient.

In the present manuscript, we shall discuss two cases in which waves formed in a string fluid in the PK-4 laboratory: (a) waves in a pure DC plasma where the microparticles were trapped by a thermal gradient, and (b) waves in an AC plasma where the polarity of the electric field is switched. This is, to our best knowledge, the first study of sound propagation in complex plasma string fluids. Hartmann *et al* [79] study waves in a superparamagnetic dusty plasma liquid and find that the sound velocity increases as the relative strength of the magnetic dipole–dipole to Yukawa interaction increases.
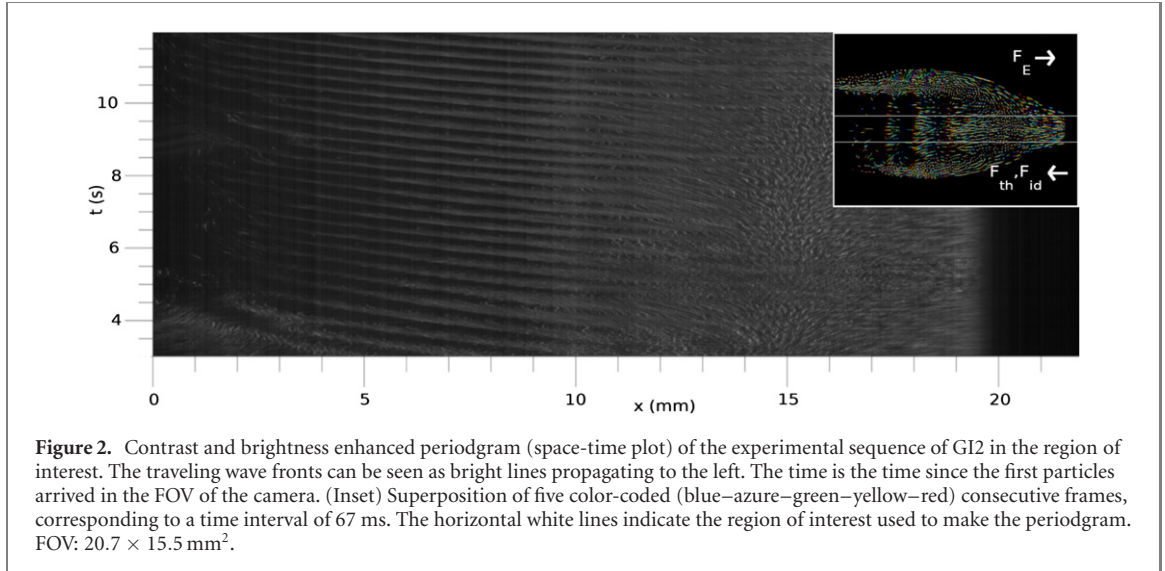
Figure 2. Contrast and brightness enhanced periodogram (space-time plot) of the experimental sequence of GI2 in the region of interest. The traveling wave fronts can be seen as bright lines propagating to the left. The time is the time since the first particles arrived in the FOV of the camera. (Inset) Superposition of five color-coded (blue–azure–green–yellow–red) consecutive frames, corresponding to a time interval of 67 ms. The horizontal white lines indicate the region of interest used to make the periodogram. FOV: $20.7 \times 15.5 \, \text{mm}^2$.

Table 1. Parameters for the parabolic flight (GI) and ISS experiments: particle diameter d_d, average microparticle density $\langle n_\text{d} \rangle$, interparticle distance Δ, neon gas pressure p, Epstein damping parameter γ_Ep, electron temperature T_e, electron density n_e, Debye length λ_D, thermal ion Mach number M_th [80], ion mean free path λ_mfp [80], and screening parameter $\kappa = \Delta/\lambda_\text{D}$. The plasma parameters are based on measurements in a particle-free plasma under the same pressure and discharge settings [42]. The microparticle densities $n_\text{d} = \Delta^{-3}$ were estimated using the position of the first peak of the pair correlation function as Δ. The ion mean free paths were calculated with a modified Frost formula for the ion mobilities [80, 81].

|	d_d (μm)	$\langle n_\text{d} \rangle$ (10^9 m^{-3})	Δ (μm)	p (Pa)	γ_Ep (s^{-1})	T_e (eV)	n_e (10^{14} m^{-3})	M_th	λ_D (μm)	λ_mfp (μm)	κ
GI1	6.8	110	210	49	063	7.8	2.6	0.55	75	73	2.8
GI2/3	3.4	170	190	49	125	7.8	2.6	0.55	75	73	2.5
ISS	3.4	125	200	38	100	7.8	2.3	0.7	80	94	2.5

3. Experimental observations

3.1. Experiments in a DC plasma during a parabolic flight

The experiments presented here (indicated with GI in the following) were performed during a parabolic flight campaign with the PK-4$^\text{GI}$ setup in spring 2019. A temperature gradient produced with the thermal manipulator stopped the particle flow in a DC plasma (DC current -1 mA, neon gas pressure 49 Pa, particles of diameter 2.1 μm, 3.4 μm, and 6.8 μm), and a force balance between electric force F_E in one direction and ion drag F_id and thermal forces F_th (namely, thermophoresis and gas drag due to thermal creep) in the other direction was established. See the inset in figure 2 for the direction of the forces.

    The temperature gradient was adjusted to the size of the injected microparticles such that particles of that specific size were trapped, but smaller ones were not. Then, smaller microparticles were injected in addition to the particles forming the existing cloud. The smaller microparticles typically arranged along the outside of the subcloud of larger particles and flowed along the edge of the cloud toward the right through the thermal manipulator. The interaction between the two particle species will be published elsewhere. Here, we only consider the dynamics of the larger particles and crop the images to the central area along the tube axis where these particles are located. Table 1 gives the experimental parameters for the three runs considered in this paper. The images were recorded at a frame rate of 60 fps and a spatial resolution of 11.8 μm/pixel.

    Figure 2 (inset) shows the superposition of particle movement during a time interval of 67 ms recorded during the experiment GI2 (parameters given in table 1). The thermal manipulator is located to the right of the image, and the electric force acting on the microparticles is directed toward the right. The ions were correspondingly streaming to the left. This lead to the formation of self-excited waves propagating in the direction of the ion flux, i.e., toward the left. The wave fronts with higher microparticle density are well visible in the image.

    We measured the wave velocities as the slopes of the wave fronts in the periodograms, such as that presented in figure 2. These space-time plots are produced by summing up all pixel intensities along the radial direction in the same central slab of the original image shown in the inset in figure 2 for each
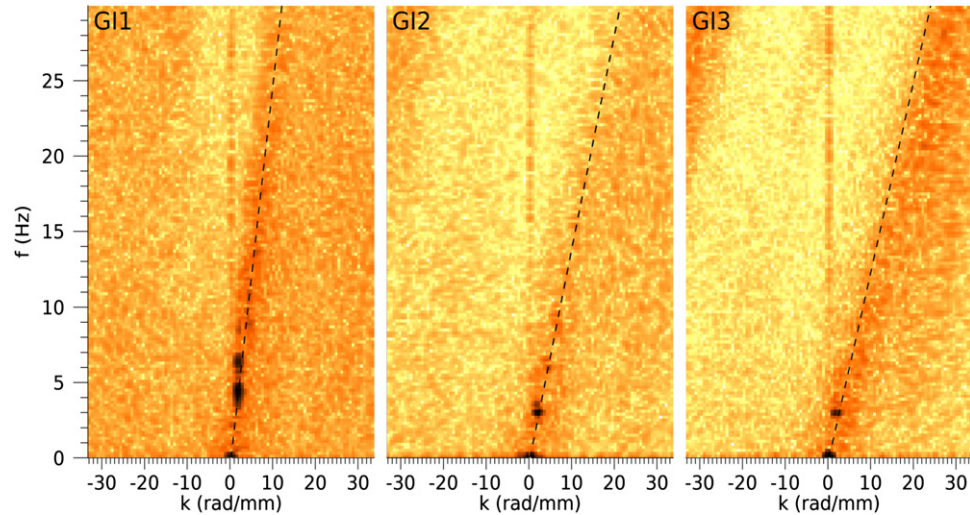
Figure 3. Spectra calculated by Fourier transform of a cropped region selected from the periodgrams of the parabolic flight experiments for maximal clarity of the spectrum (GI1: $0.0\ \text{mm} \leqslant x \leqslant 9.4\ \text{mm}$, $3.3\ \text{s} \leqslant t \leqslant 8.3\ \text{s}$, GI2: $5.0\ \text{mm} \leqslant x \leqslant 14.4\ \text{mm}$, $5.0\ \text{s} \leqslant t \leqslant 10.0\ \text{s}$, GI3: $1.2\ \text{mm} \leqslant x \leqslant 10.6\ \text{mm}$, $5.0\ \text{s} \leqslant t \leqslant 10.0\ \text{s}$). The overplotted lines correspond to velocities of GI1: $16\ \text{mm s}^{-1}$, GI2: $9\ \text{mm s}^{-1}$, and GI3: $8\ \text{mm s}^{-1}$. The position of the brightest harmonics in GI1 is at 4.5 Hz and 6.5 Hz, and for GI2 and GI3 at 3 Hz.

horizontal position x (i.e., using a bin size of 1 pixel in the horizontal direction) [68]. The resulting intensities are a function of the axial position and time, and are used as gray-scale values for the periodgrams. The brighter regions correspond to higher particle density [82] and, in the case of waves, to the wave ridges. The slopes of the wave fronts correspond to their velocity. Another way to determine the wave velocities is to calculate the spectra by Fourier transformation of a cropped region of the periodgrams. These are shown in figure 3.

For the runs GI2 and GI3, the waves slowed down significantly as they traveled to the left—this can be discerned as an increase in slope (i.e., the wave fronts need longer time as they travel a certain distance) closer to the left edge of the picture in the periodgram (figure 2). However, it is not immediately clear whether this is a result of string formation, or some other effect such as variation of local electric field [17]. Analyzing the particle positions in this experiment is difficult due to their high streaming velocity. Also, the influence of the vortices induced by thermal creep complicates the analysis. In section 4, we shall compare the measured wave velocities to the theoretically expected ones. Before that, we shall present experiments performed with the ISS setup, in which the microparticles were trapped by polarity switching, leading to bipolar wakes in contrast to the unipolar wakes in the parabolic flight experiment. In these experiments the microparticles were easier to trace than in the Gießen experiments.

## 3.2. Experiments with polarity switching on board the ISS

The experiment presented here was performed during the commissioning of the PK-4 laboratory. The gas flux (from left to right in the PO images) was 0.05 sccm in neon gas at a pressure of 38 Pa. Melamine formaldehyde microparticles of diameter 3.37 μm and a mass of 3.0×10^{-14} kg were injected into the plasma, and their position was stabilized by driving the plasma in polarity switching mode at a frequency of 500 Hz with a duty cycle of 50% [42] at discharge current of 1.0 mA and a voltage of 770 V. The corresponding experimental parameters measured in a microparticle-free plasma [42] are given in table 1. The recording frame rate in the experiment was 35 fps for the PO cameras and 25 fps for the plasma glow camera. Using the electric field measured in the particle-free plasma, $E = 218\ \text{V m}^{-1}$ [42], and a modified Frost's formula [80, 81] results in a thermal Mach number of the ions of $M_{\text{th}} = 0.7$.

Under these conditions, a large cloud of microparticles was visible in the PO cameras, see figure 4, and the movie CombinedImages.mp4 in the supplemental materials (https://stacks.iop.org/NJP/22/083079/mmedia). The cloud was overall stationary in the FOV of the PO cameras. Long axial strings developed due to the polarity switching of the discharge electric field, as is easily visible in the original image (figure 4 top). On the left of the visible microparticle cloud, stable self-excited waves developed which propagated to the left. Toward the right edge of the cloud, waves were also sometimes visible, propagating in the same direction as those on the left, but not with the same regularity.

Figure 4 (bottom) shows the detected particles corresponding to the top image in the same figure, color-coded by each particle's anisotropic weighted scaling index. A scaling index close to 1 indicates a
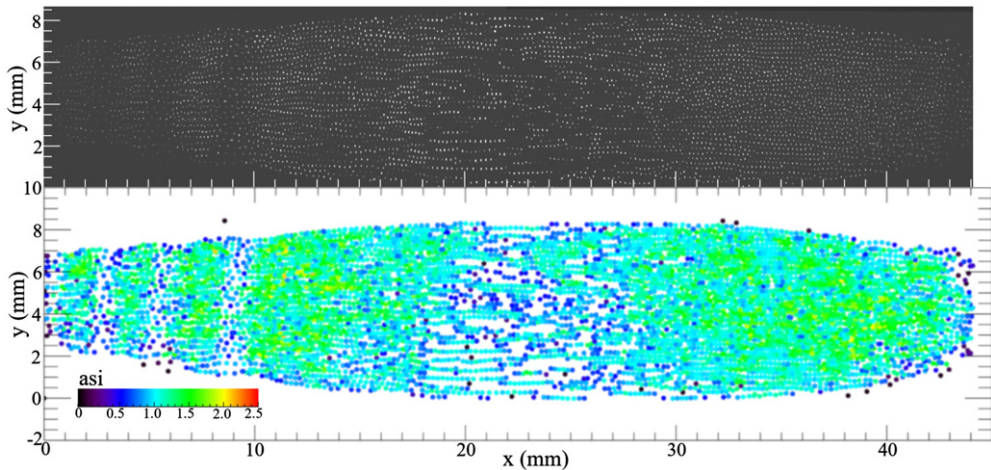
Figure 4. (top) Contrast and brightness enhanced image recorded with the PO cameras in the ISS experiment, combined into one image as described in [50], with superposed coordinate system. The waves are located mainly at the left side, at $x \lesssim 20$ mm. (bottom) Positions of identified particles in the same frame, color coded by local longitudinal weighted anisotropic scaling index (asi) calculated with the values $R = 0.3$ mm, aspect ratio $= 5$ (see appendix A for details). The fact that the scaling index differs from 1 in the denser parts of the clouds, such as the wave ridges, shows that a different scale R is needed there as compared to the central part of the cloud.
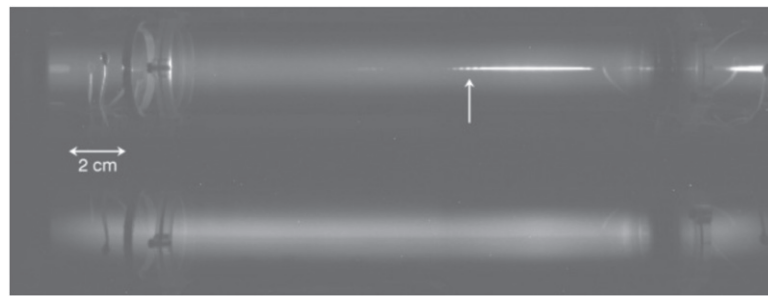

Figure 5. Contrast enhanced view of the plasma glow in the ISS experiment. (top) Spectrum-integrated view including the light from the illumination laser (bright axial white line). The arrow indicates the location of the waves visible at the left side of the FOV of the PO cameras. (bottom) Filtered view (filter transmitting the neon line at 585.2 nm with a spectral width of 8.2 nm). A movie is available in the supplemental materials.

string-like structure seen at a given scale R, one closer to 0 a point-like structure, and one closer to 2 a planar structure [83] (see appendix A for details on the scaling index). For the parameters selected in figure 4, the scaling index is close to 1 (azure color in the figure) in the central area of the cloud (near $x = 20$ mm), which is also where the most prominent strings are visible with the naked eye. Inside the denser wave ridges to the left, the scaling index is larger (green color in the figure), which is probably due to improperly selected scale R compared to the interparticle distance in that region.

Figure 5 shows two of the channels recorded with the glow camera. The top shows the unfiltered channel, so the light of the illumination laser reflected by the microparticles is visible. The line of sight of the glow camera is parallel to the illuminated plane. The vertical arrow indicates the position of the waves visible with the PO cameras. A little further to the left, there is another subcloud of particles, in which waves are traveling in the same direction as those in the PO FOV (see movie glow.mp4 in the supplemental materials). The same holds for another subcloud of particles trapped to the right of the cloud visible in the PO FOV.

The bottom panel of figure 5 shows only the light emitted by the neon plasma. No obvious striations are visible, and there are also no patterns corresponding to the waves in the microparticle cloud. Nevertheless, a local time-averaged electric field must be present, as is indicated by the fact that the microparticles are trapped in the tube despite a gas flow, and by the fact that waves are observed, which are usually excited by ions streaming through a microparticle cloud [15]. Using equation (4), a critical electric field of $E_{\text{crit}} = 120$ V m^{-1} would be required to excite waves. With the diagnostics available in the ISS laboratory, we cannot measure the electric field *in situ*. It is well known that the presence of microparticles can strongly
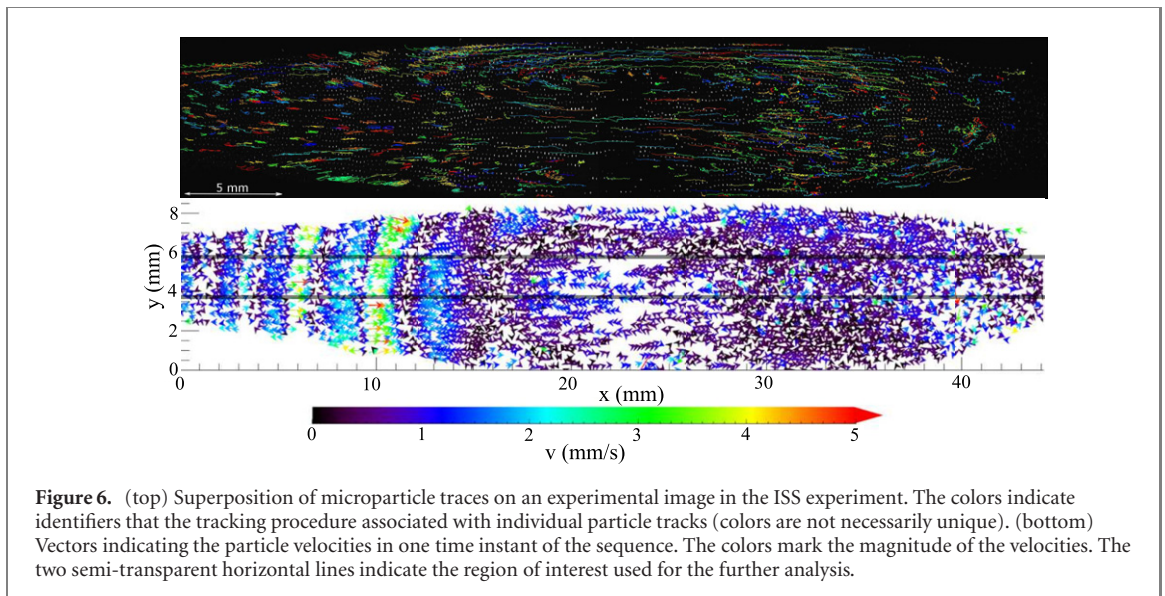
Figure 6. (top) Superposition of microparticle traces on an experimental image in the ISS experiment. The colors indicate identifiers that the tracking procedure associated with individual particle tracks (colors are not necessarily unique). (bottom) Vectors indicating the particle velocities in one time instant of the sequence. The colors mark the magnitude of the velocities. The two semi-transparent horizontal lines indicate the region of interest used for the further analysis.

influence the plasma [84–88], and that striations can influence waves [89]. Simulations such as those presented by Zobnin *et al* [90] would be useful, but are beyond the scope of the present paper.

We traced the microparticles from frame to frame in the PO cameras using standard methods of identifying particles by pixel brightness above a threshold and linking their trajectories [91, 92]. The top panel of figure 6 shows typical particle tracks superposed on a combined experimental image. It can be seen that the microparticles in the center of the cloud move toward the left and back around the vertical edges of the cloud toward the right, with some modulation due to the waves. The bottom panel in figure 6 shows the velocity vectors of an exemplary video frame (see vels_v.mp4 in the supplemental materials for a movie). The waves are clearly visible.

In contrast to typical dust-acoustic waves [68], the wave ridges/fronts (i.e., the regions where the microparticle number density is elevated, and the particles move in the same direction as the waves) were much wider than the wave troughs. The particles moved faster in the wave troughs than in the wave ridges. In the supplemental materials, there is a movie which shows the median axial and radial velocities averaged with a sliding window of 10 pixel radius and over ten frames (vx_10p.mp4 and vy_10p.mp4). These movies demonstrate the movement of microparticles in the waves ridges, the emergence of the waves near the center of the cloud, some waves near the right edge of the microparticle cloud, and occasionally a pulse of negative particle velocities (dark in vx_10p.mp4) originating at the center of the cloud and moving toward the right.

The shape of the waves is also visualized in figure 7, which shows a typical wave form, the envelope functions of the wave forms and the mean axial velocity as a function of axial position. The velocity of the particles peaks at around $x = 8$ mm and then reduces toward the cloud edge. Using plots like the waveform shown in figure 7, we trace the propagation of the wave ridges and troughs by following the extreme values of the wave form through time and space. The wave velocity is calculated from the distance that the maxima and minima moved from frame to frame. The peaks move mainly with velocities of $-(3–7)$ mm s^{-1}, while the particles move with about -1 mm s^{-1} in the wave ridges and 2 mm s^{-1} to 4 mm s^{-1} in the wave troughs.

Next, we shall study the spectral properties of the observed waves. In order to do so, we calculate periodograms by calculating the sum over the radial direction of all pixel intensities in the same slab used to calculate the velocities shown in figure 7 (3.75 mm $\leqslant y \leqslant$ 5.75 mm). The resulting total intensities, which are a function of the axial position x and time t, are used as gray-scale value for the image shown in the middle panel in figure 8. The microparticle density is roughly proportional to the image brightness [82] (if recorded with the same camera and the same illumination intensity, so this is not necessarily true here since images from two cameras were combined, and the width of the laser changes as a function of axial position x). The wave ridges are well visible as brighter regions in the left part of the cloud, corresponding to higher density regions.

A more precise way to measure the microparticle number density is to measure the interparticle distance Δ. We calculated Δ in the same radial slab as before by determining the position of the largest peak of the pair correlation function $g(r)$, again as a function of axial position (with a step size of 0.1 mm) and time, and using particles with x-positions within 1 mm from the currently considered position. We show the
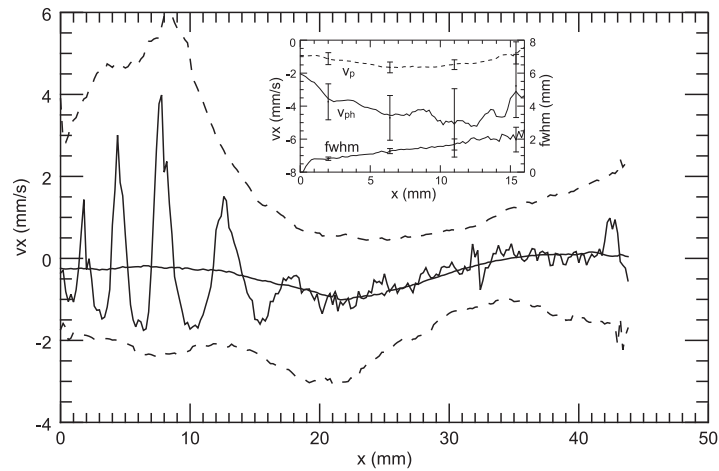
Figure 7. Typical waveform (mean axial velocity in one frame averaged in bins of 0.2 mm width in x direction and in the range $3.75\,\text{mm} \leqslant y \leqslant 5.75\,\text{mm}$, solid line) and smoothed envelope functions (dashed lines) of all waveforms as a function of axial position in the ISS experiment. The dotted line is the mean axial particle velocity in the given region averaged over all frames. (inset) Average phase velocity v_{ph}, solid line, and particle velocity v_{p}, dashed line, as well as the full width at half maximum of the velocity peaks that could be fitted by a Gaussian, dotted line, of the waves resp. particles moving leftwards in the region $x \leqslant 16\,\text{mm}$, where the waves are well-pronounced.
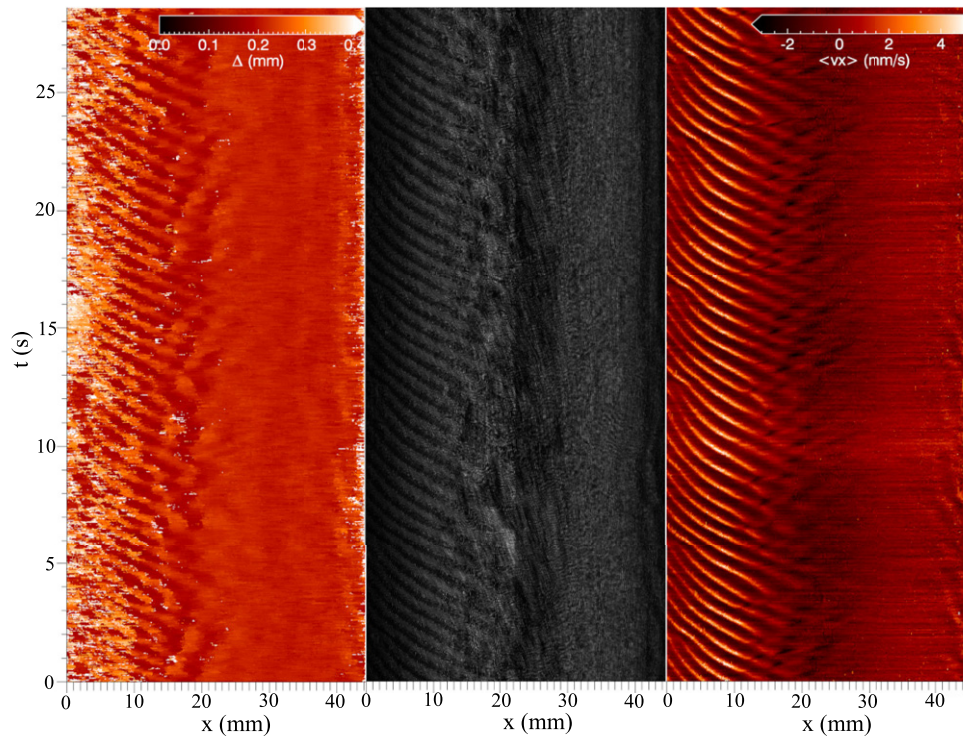
Figure 8. Space-time plots (periodograms) of the ISS experiment calculated using three different methods. In each panel, data are shown as a function of axial position x and time t, averaged in radial position in the slab $3.75\,\text{mm} \leqslant y \leqslant 5.75\,\text{mm}$. (Left) Interparticle distance measured with the largest peak in the pair correlation function. (Center) Periodogram calculated from original images. (Right) Mean axial velocity. Note that only in the middle panel a clear transition between the regions recorded with the two cameras is visible.

result in the left panel in figure 8. Inside the wave ridges, $\Delta_{\text{r}} \approx 180\,\mu\text{m}$, and in the troughs, $\Delta_{\text{t}} \approx 300\,\mu\text{m}$. These values are comparable with dust density waves in complex plasmas without strings, e.g., in [68], $\Delta_{\text{r/t}} = 173/295\,\mu\text{m}$ for waves formed in a cloud of $1.28\,\mu\text{m}$ diameter particles.

Interestingly, in the Δ-periodogram several features emerge that are not visible in the image-periodogram: in the central region ($15\,\text{mm} \lesssim x \lesssim 27\,\text{mm}$) large-scale structures propagating toward the right appear, and at the right cloud edge, additional waves moving left similar to those at the left cloud edge are visible. The
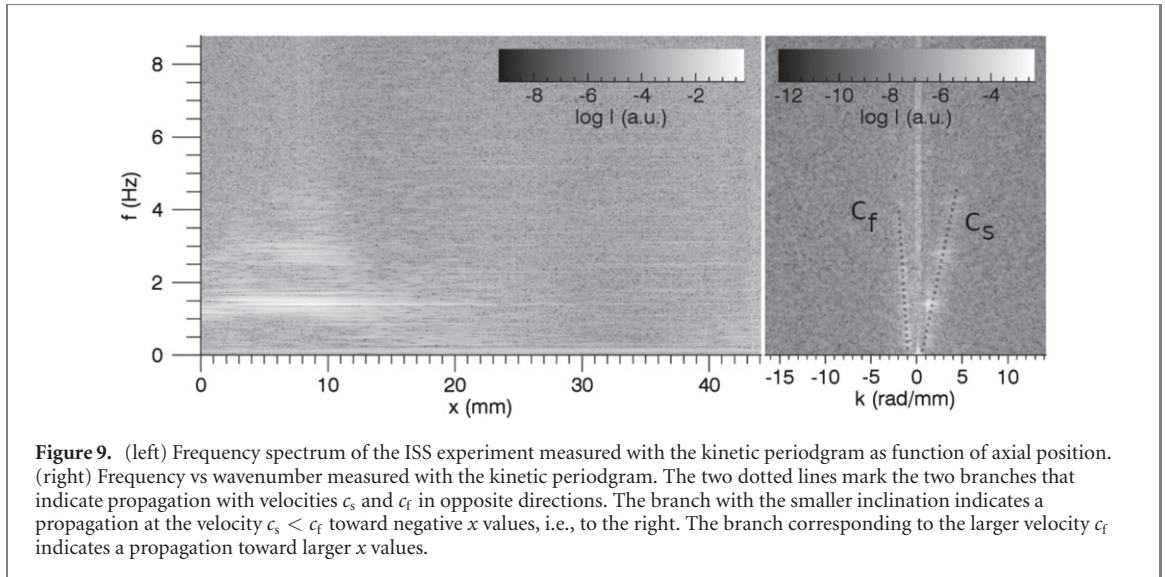
Figure 9. (left) Frequency spectrum of the ISS experiment measured with the kinetic periodogram as function of axial position. (right) Frequency vs wavenumber measured with the kinetic periodogram. The two dotted lines mark the two branches that indicate propagation with velocities c_s and c_f in opposite directions. The branch with the smaller inclination indicates a propagation at the velocity $c_s < c_f$ toward negative x values, i.e., to the right. The branch corresponding to the larger velocity c_f indicates a propagation toward larger x values.

features are also easily distinguishable in the movie in the supplemental material showing the median axial velocity (vx_10p.mp4).

In the right panel of figure 8, a periodogram is calculated from the mean axial velocity of the particles located inside the slab, using a bin size of 0.1 mm in axial (x) direction. All features seen in the Δ-periodogram also appear in this 'kinetic' periodogram.

In order to study the spectral properties, we calculated a Fourier transform across the time dimension of the kinetic periodogram, see figure 9(a). The waves in the right side of the image are well visible with the fundamental frequency $f = 1.4$ Hz and its harmonics. In the 1D power spectrum, the signal vanishes around $x = 24$ mm, which is the region where the waves originate. Figure 9(b) shows the two-dimensional (2D) Fourier transformation of the kinetic periodogram. Interestingly, two branches are visible, which correspond to signals with velocities $c_f = 22$ mm s^{-1} and $c_s = 6$ mm s^{-1}. The slow velocity, c_s, corresponds approximately to the wave velocity that we measured above. In order to determine where the fast branch originates, we mask the region of the Fourier transformed spectrum outside of the c_f branch and then perform an inverse Fourier transform. This allows us to identify that this signal originates from the features with large negative horizontal velocity around 16 mm $< x <$ 25 mm. The velocity of the fast branch corresponds very well to that theoretically expected for the case without attractive interactions, as we shall see below.

4. Discussion

The origin of the wave harmonics seen in the spectra (figures 3 and 9) is an interesting point to speculate about. They can be connected to the inhomogeneities of the local electric field. For a quick estimate for the ISS experiment, we assume that locally there is a balance between the counteracting forces from the gas flowing at velocity v_{gas} and that from the local average electric field E_x, in analogy to gas flow compensating for the force of gravity [23] (for the Gießen experiments, the thermal forces would need to be considered, and in both cases we are neglecting the ion drag force for this estimate). Considering a particle with mass m_d and charge Z_d at the equilibrium point, we get

$$m_d \gamma_{Ep} v_{gas} \sim Z_d eE \rightarrow E \sim 20 \text{ V m}^{-1}, \tag{7}$$

where we used the neutral gas velocity $v_{gas} = 3$ mm s^{-1}. Then, if a particle happens to be located a small distance away from the equilibrium point, it is subjected to a force

$$m_d d^2 x/dt^2 = +Z_d eE'_x x$$

with axial position x and local electric field gradient E'_x. This corresponds to a stable oscillation with the frequency f_{fund}:

$$(2\pi f_{fund})^2 = \left| Z_d eE'_x/m_d \right|. \tag{8}$$

Table 2. Estimated particle charge number Z_d calculated from the reduced charge $z = 0.3$ [52], theoretically expected wave velocity $c_{DA,c}$ calculated with the customary equation (5) and the parameters given in table 1, theoretically expected wave velocity $c_{DA,s}$ calculated with the velocity scale, equation (6) [77], and average measured wave velocities c_{exp} and their standard deviations for the experiments as well as the velocities measured with the spectra, c_{spec}. For the GI experiments, c_{exp} was measured from the slopes of the wave fronts in the periodograms, for the ISS experiment, the peaks in particle velocity were traced (see figure 7). Please note that for GI2 and GI3, the waves slowed down significantly as they traveled to the left, which is the region where the spectra were measured.

	Z_d	$c_{DA,c}$ (mm s^{-1})	$c_{DA,s}$ (mm s^{-1})	$\langle c_{exp} \rangle$ (mm s^{-1})	c_{spec} (mm s^{-1})
GI1	5500	14.6	12.6	15 ± 6	16
GI2	2800	25.0	21.7	11 ± 4	9
GI3	2800	25.0	21.7	12 ± 7	8
ISS	2800	24.2	21.6	$3-7$	6

Solving for E'_x with the parameters of the ISS experiment results in $E'_x = 0.5$ V cm^{-2}. Using equations (7) and (8) results in the typical length scale L

$$Z_d e E \sim Z_d e E'_x L \rightarrow L \sim 4 \text{ mm}. \tag{9}$$

The length scale $L \sim 4$ mm corresponds very well to the observed wave length, suggesting that there is possibly a resonance between this mode and the sound waves.

The presence of harmonics is also an indication of non-linearity in the waves [72, 93]. The degree of non-linearity ϵ can be estimated using a hydrodynamical relationship:

$$\epsilon = n_1/n_0 = v_1/c, \tag{10}$$

where the index 1 indicates the perturbed and 0 the unperturbed state, c the speed of sound and v the velocity. Using, e.g., figure 7 to get $\max(v) = +4$ mm s^{-1} and $\min(v) = -2$ mm s^{-1}, and $c_f = 22$ mm s^{-1} and $c_s = 6$ mm s^{-1} results in
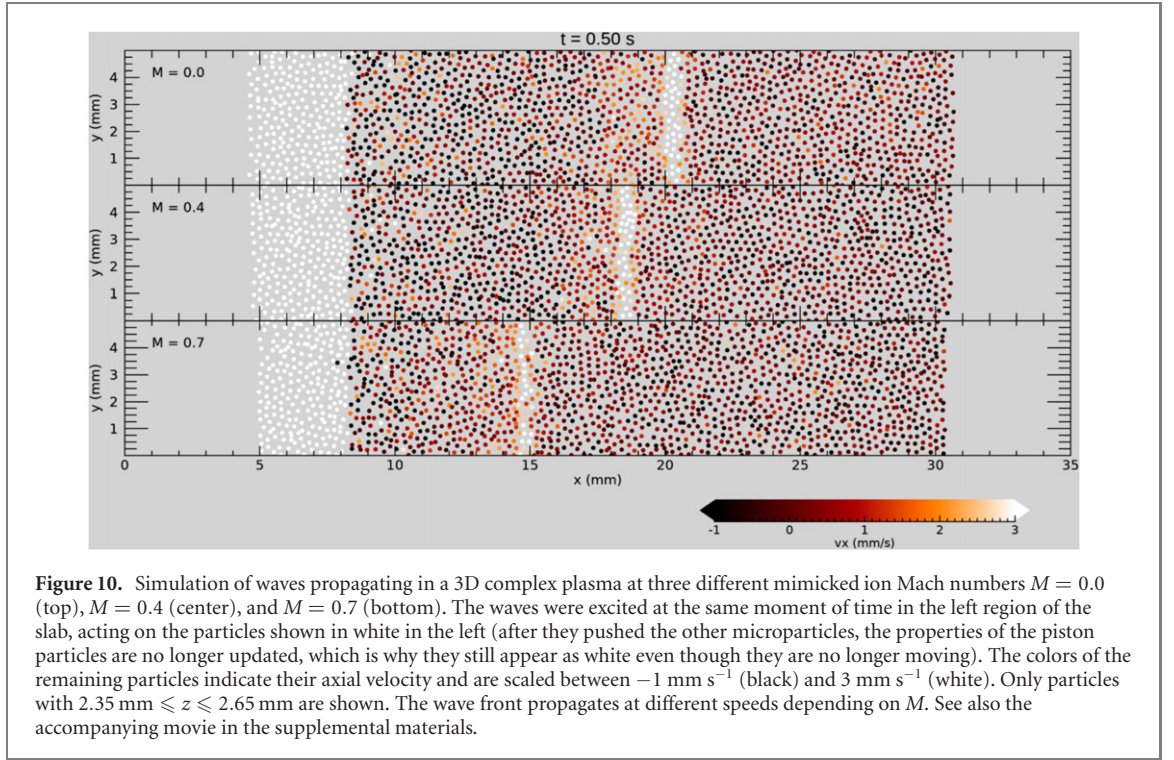
$$\epsilon = 1/5 - 1/3 < 1. \tag{11}$$

Similarly, the increase in intensity in the periodogram figure 8 (middle), which is proportional to the increase in density, is maximally 30% in the wave crests compared to the mean intensity/density, and the harmonics in the spectrum (figure 9) suggest a similar relationship. Therefore, we conclude that the waves in our case are only weakly non-linear, and the linear theory describes the experiments reasonably well.

Table 2 gives the charge number, based on the measured dimensionless charge $z = 0.3$ [52], and experimentally measured wave velocities for all four experimental runs. We compare these wave velocities with the conventional theoretical wave velocity $c_{DA,c}$ based on equation (5) and that based on the velocity scale $c_{DA,s}$, equation (6), using equation (21) from reference [77]. It can be seen that the theoretically expected velocity is faster than the experimentally measured one in all cases except for the GI1 experiments in which larger particles were used. There, both theories predict velocities in the range of the experimentally determined one. We believe that the waves in these experiments are not slowed due to a decreased influence of the strings, but since we cannot trace the microparticles reliably in this experiment, the test of this hypothesis will need to be done in a future experiment. The most significant difference between the expected and measured wave velocities occurs in the case of the ISS experiment, in which polarity switching leads to the formation of bipolar wakes, compared to the unipolar case of the parabolic flight experiments GI1−GI3.

These results suggest the hypothesis that the additional attractive force in ER plasmas leads to a decrease of the dust acoustic wave velocity. In order to test this hypothesis, we performed molecular dynamics (MD) simulations for both 2D slabs of size 35×5 mm^2 and 3D rectangular cuboids of size $35 \times 5 \times 5$ mm^3 with microparticles of 3.4 μm diameter and a charge of 5500e each. The microparticles interacted with each other via Yukawa potential and two additional, positively charged point charges positioned along the tube axis in order to mimic the wakes formed by ion streams. The strength and position of these point charges depended on the assumed ion Mach number. The microparticles were also subject to random kicks, mimicking the transfer of temperature from the background gas, and to gas drag—however, the gas pressure was set to only 0.38 Pa in order to facilitate the propagation of waves. See appendix B for details.

Instead of simulating self-excited dust density waves, we performed a simpler experiment by pushing the microparticles from the left side with a piston consisting of other microparticles, similar as in [94]. This lead to a propagation of a wave through the microparticle cloud. The piston particles only moved a short

Figure 10. Simulation of waves propagating in a 3D complex plasma at three different mimicked ion Mach numbers $M = 0.0$ (top), $M = 0.4$ (center), and $M = 0.7$ (bottom). The waves were excited at the same moment of time in the left region of the slab, acting on the particles shown in white in the left (after they pushed the other microparticles, the properties of the piston particles are no longer updated, which is why they still appear as white even though they are no longer moving). The colors of the remaining particles indicate their axial velocity and are scaled between -1 mm s^{-1} (black) and 3 mm s^{-1} (white). Only particles with $2.35\,\text{mm} \leqslant z \leqslant 2.65\,\text{mm}$ are shown. The wave front propagates at different speeds depending on M. See also the accompanying movie in the supplemental materials.

distance of the order of 100 μm, in contrast to simulations in which the piston moves continuously, e.g., [95].

Figure 10 shows the microparticle positions in a central slice of width 300 μm in z direction, color-coded with their velocity, at the same instant of time after the push with the piston. It can be seen that the soliton propagated faster for runs with lower mimicked Mach numbers of the ions, M, even though string formation was not strong under the conditions of this simulation run. The same difference in propagation velocity was observed in all simulation runs in 2D and 3D and at various microparticle temperatures and number densities. Thus, these simulations support our hypothesis that the extra anisotropic attraction causes a slowing of the propagation of waves. Next, we shall calculate the expected velocity of sound analytically.

A reduction of the wave sound velocity with the ion flow speed in a 1D ER complex plasma lattice with dipole-like interactions has been predicted theoretically by Rosenberg [96]. We have performed a similar calculation, based on the plasma and particle parameters relevant for the ISS experiment in our present study. Please note that this calculation does not apply to the unipolar attraction in the Gießen experiments. Some clarifying details are provided below.

The sound velocity of an ideal 1D lattice can be expressed as a sum over lattice sites involving the second derivative of the pairwise interaction potential. It is, therefore, additive in the sense that if the potential can be presented in the form

$$\phi(r) = \sum_i \phi_i(r),$$

then the corresponding sound velocity is

$$c_s^2 = \sum_i c_{s,i}^2.$$

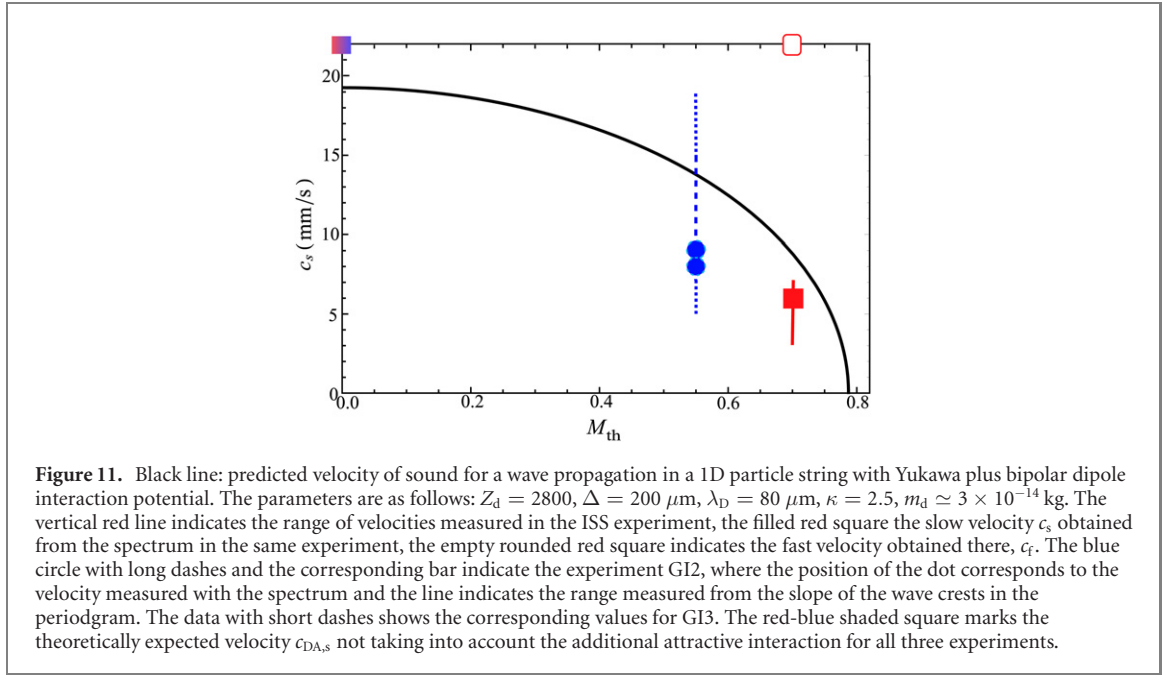Consider now the 1D chain of particles interacting via the potential

$$\phi(r) = \phi_Y(r) + \phi_D(r),$$

where ϕ_Y and ϕ_D are given by equations (2) and (3), respectively. The infinite summation over lattice sites can be easily performed for each of the potentials. We quote the final result

$$c_Y^2 = c_0^2 \left\{ \frac{\kappa e^\kappa [\kappa - 2 + 2e^\kappa]}{(e^\kappa - 1)^2} - 2\,\ln(e^\kappa - 1) \right\},$$

and

$$c_D^2 = -12.38 c_0^2 \left(\frac{M_{\text{th}}}{\kappa} \right)^2. \tag{12}$$

Figure 11. Black line: predicted velocity of sound for a wave propagation in a 1D particle string with Yukawa plus bipolar dipole interaction potential. The parameters are as follows: $Z_d = 2800$, $\Delta = 200$ μm, $\lambda_D = 80$ μm, $\kappa = 2.5$, $m_d \simeq 3 \times 10^{-14}$ kg. The vertical red line indicates the range of velocities measured in the ISS experiment, the filled red square the slow velocity c_s obtained from the spectrum in the same experiment, the empty rounded red square indicates the fast velocity obtained there, c_f. The blue circle with long dashes and the corresponding bar indicate the experiment GI2, where the position of the dot corresponds to the velocity measured with the spectrum and the line indicates the range measured from the slope of the wave crests in the periodogram. The data with short dashes shows the corresponding values for GI3. The red-blue shaded square marks the theoretically expected velocity $c_{DA,s}$ not taking into account the additional attractive interaction for all three experiments.

The resulting sound velocity is just the sum of these two contributions, $c_s^2 = c_Y^2 + c_D^2$.

    Figure 11 shows the theoretically calculated sound velocity in a 1D complex plasma as a function of the thermal ion Mach number for 3.4 μm particles and relevant plasma parameters for the ISS experiment. It can be seen that the wave velocity decreases dramatically with the Mach number, up to $M_{th} \simeq 0.8$, above which no more wave propagation is possible. The lattice becomes unstable in this regime. The experimental results for the slow branch in the ISS experiment, and the wave speed in the GI2/3 experiments are also shown in the graph for reference with solid symbols (remember that no close match is expected since the theory describes bipolar wakes as in the ISS experiment, not unipolar wakes as in the Gießen experiments, and the theory is 1D, while the experiments are 3D). The empty red square indicates the fast velocity measured in the ISS experiment, and the red-blue shaded square the theoretically expected velocity for all three experiments when no wakes are present in the system. The fit of the experimental data to the graph is well visible. For the ISS experiment, the measured wave velocity of 3–7 mm s^{-1} corresponds to $M_{th} \simeq 0.75$ in this simple calculation, which is very close to the value in the experiment, $M_{th} = 0.7$. The origin of the sound velocity reduction is the attractive interaction between the particles, which is also responsible for the formation of string-like structures.

    Going back to equation (12), we can associate the slow branch measured in the ISS experiment with c_s and speculate that the 'normal' (unaffected by wakes) sound velocity corresponds to the fast branch observed in the spectrum, $c_Y = c_f$. This results in

$$c_s{}^2 = c_f{}^2 + c_d{}^2, \tag{13}$$

$$c_d{}^2 = -M_{th}{}^2 c_{cor}{}^2, \tag{14}$$

where c_{cor} is the proportionality coefficient which can be determined as

$$c_{cor} = \sqrt{(c_f^2 - c_s^2)/M_{th}{}^2} \sim 30 \text{ mm s}^{-1}. \tag{15}$$

In order to test how well the 1D theory describes the 3D data, we compare the proportionality factor α that gives $-c_D^2$ as a function of c_0, M_{th} and κ,

$$-c_d^2 = \alpha^2 (c_0 M_{th}/\kappa)^2. \tag{16}$$

For the experimental (3D) data, equation (14) results in

$$\alpha_{3D} = c_{cor}\,\kappa/c_0 \sim 4.3, \tag{17}$$

which is within 20% of the α-factor calculated for the 1D string above, $\alpha_{1D} = \sqrt{12.38} = 3.5$. Thus, the 1D description fits our data with about 20% accuracy.

5. Summary

In conclusion, we studied the propagation of waves in weightless complex plasmas forming strings using experiments during a parabolic flight and on board the International Space Station. During the parabolic flight, strings form in a DC plasma with unipolar wakes. In the ISS experiment, the strings form in a plasma where the polarity of the electrodes is regularly switched, leading to bipolar wakes. In that case, the wave troughs are narrower and the crests broader compared to ordinary dust density waves. The wave phase velocity decreases with respect to that expected for a string-free complex plasma. Supporting MD simulations of bipolar wakes show that the wave velocity depends on the strength of the formed wakes. This finding was also reproduced in theoretical considerations of waves propagating in a 1D complex plasma with bipolar wakes, and likely also occurs in other string-forming systems. In the future, a more realistic wake model [97] will be incorporated in the simulations, and more detailed studies of the wave velocity as a function of the ion Mach number and of the rheology of ER plasmas are planned using both the PK-4^{GI} setup during parabolic flights and the PK-4 laboratory on board the ISS.

Acknowledgments

Appendix A. Anisotropic scaling index

The dimensionality of the local structure around each point that is discernible at a certain scale a can be characterized by the scaling index α [98, 99]. For example, a local structure that, at the scale a, 'looks' like a point has a scaling index $\alpha \simeq 0$, one that looks like a line, $\alpha \simeq 1$, and one that looks like a plane, $\alpha \simeq 2$.

A linear approximation of α for a point $\boldsymbol{x}_i$ embedded in a cloud of particles is given by

$$\alpha(\mathbf{x}, r_1, r_2) = \frac{\ln\ N(\mathbf{x}_i, r_2) - \ln\ N(\mathbf{x}_i, r_1)}{\ln\ r_2 - \ln\ r_1}, \tag{A.1}$$

where $N(\mathbf{x}_i, r)$ is the number of the particles within a distance r of $\mathbf{x}_i$ (the 'local mass'), and r_1 and r_2 are two radii with $r_1 < r_2$. The two radii should be selected such that the scale of the structures of interest is captured.

Anisotropic structures can be examined by projecting the local masses on a vector of interest (most commonly the axes) [98, 100], so that

$$N_t(\mathbf{xi}, r_1, r_2) = \sum_{j=1}^{k} \Theta(r_1 - \|x_i{}^t - x_j{}^t\|) - \Theta(r_2 - \|\mathbf{x}_i - \mathbf{x}_j\|), \tag{A.2}$$

where t indicates the projection on the vector of interest, and Θ is the Heaviside function. The *anisotropic scaling index* α_i is then determined with equation (A.1) using the projected local masses N_t instead of N. It contains information on the orientation of the detected structures with respect to the vector of interest.

The *weighted anisotropic scaling indices* determine the cumulative point distribution using Gaussian weights and a single scale R, no longer the Heaviside function, resulting in the following impression for α [83]

$$\alpha(\mathbf{x}, R) = \frac{\sum_{j=1}^{k} 2(d_{ij})^2\ \exp\left[-(d_{ij}/R)^2\right]}{\sum_{j=1}^{k}\ \exp\left[-(d_{ij}/R)^2\right]}, \tag{A.3}$$

where d_{ij} are the weighted distances between microparticles i and j

$$d_{ij} = \left[\lambda_x{}^2(x_i - x_j)^2 + \lambda_y{}^2(y_i - y_j)^2\right]^{1/2}. \tag{A.4}$$
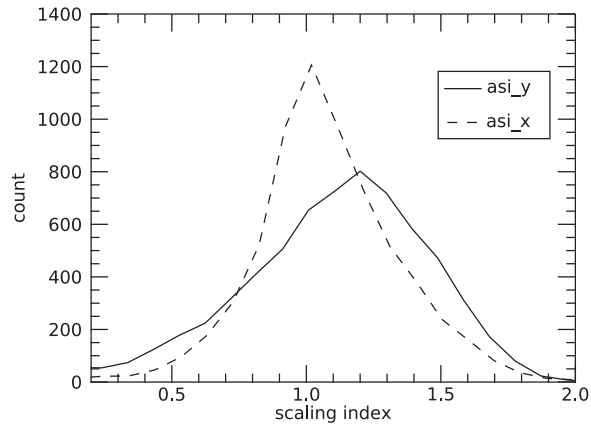
Figure A1. Distribution of weighted anisotropic scaling indices in x (asi_x) and y (asi_y) directions for the ISS experiment, corresponding to the particle distribution shown in figure 4. It is clearly visible that the particle distribution is more string-like in the x direction compared to the y-direction.

Typically, to detect structure formation along the x-axis, $\lambda_x = 1$ and $\lambda_y = \lambda_z = 5$ are chosen [83], with appropriate permutations for detection of strings along the other axes. The scale R can be defined by the interparticle distance [57]. For the ISS experiment, we used $R = 0.3$ mm. Figure A1 shows the distribution of weighted anisotropic scaling indices in the ISS experiment.
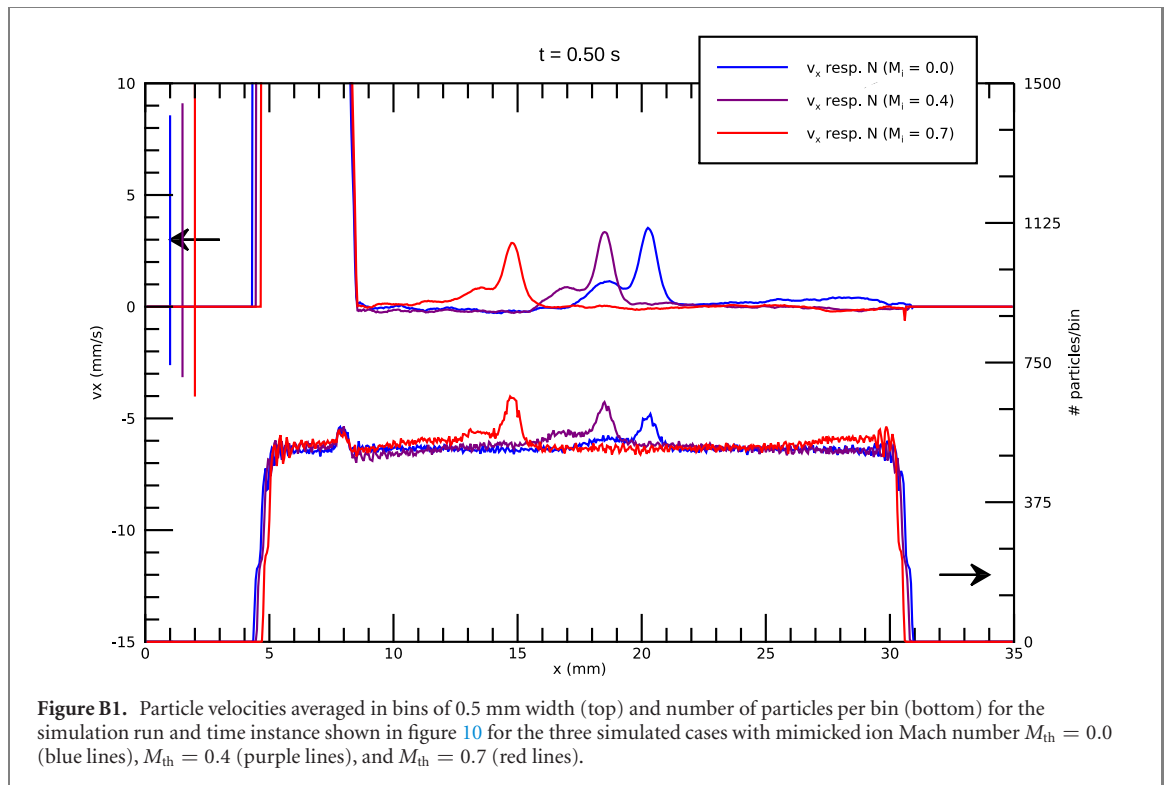
Appendix B. Simulations

In order to test the hypothesis that the reduced wave velocity is an effect of the string formation in the complex plasma fluid, we performed numerical simulations. We did not simulate self-excited dust acoustic waves since these waves stem from a complicated interaction between the microparticles and plasma ions, a self-consistent simulation of their excitation is beyond the scope of this paper. Instead, here we simulate the propagation of a soliton produced by a push with a 'piston'. For this purpose, we use the MD simulator LAMMPS [101], which we modified to model effective dipoles induced by the wakes as a function of the ion Mach number. Other than in our previous publications [102, 103], we did not explicitly simulate the background plasma, but only took it into account implicitly via the assumed screened interaction potential between the charged microparticles.

We ran both 2D simulations with a box of size 35×5 mm² with a harmonic confinement at the x edges and periodic boundary conditions along the y direction and 3D simulations with a box of size $35 \times 5 \times 5$ mm³ with a harmonic confinement at the x edges and periodic boundary conditions along the y and z directions. We used a screening length $\lambda_D = 80$ μm, microparticles of diameter $d_d = 3.37$ μm with a charge of $Q_d = 5500e$ each, where e is the electron's charge. Note that this charge corresponds to that calculated for the given plasma parameters using the theory presented in [53], not to the experimentally measured charge [52] that was used for the analysis of the experiments.

The gas pressure (used to calculate the damping coefficient and to control the effectiveness of setting the microparticles' temperature) was set to only 0.37 Pa, two orders of magnitude smaller than the experimental one, to allow for transmission of a soliton without continuous energy input from ions as is the case for dust acoustic waves. We included the influence of the neutral background gas by using a Langevin equation—the microparticles were subject to random pushes of assumed neon atoms depending on the selected microparticle temperature. The microparticles were also subjected to Epstein drag when moving relative to the gas [104], the strength of which is given by the Epstein drag coefficient. The microparticles interacted via Yukawa potential. For the 2D simulations, the interaction potential was truncated at 5 mm, for the 3D ones, at 2 mm due to computational limitations.

In order to mimic the effective dipole potential (equation (3)) induced by the ions streaming past the microparticles, we first attempted to incorporate the effective dipole interaction (equation (3)) directly. This approach turned out to be numerically unstable, with the simulated microparticles undergoing large accelerations due to close encounters with another microparticle even at very small time steps. An approach that is more promising is to incorporate an analytic potential [105] as was done by Kana for high thermal Mach numbers [106]. However, since the simulation in the present paper only serves as test of our hypothesis that the formation of strings slows down the propagation of waves and does not attempt to

Figure B1. Particle velocities averaged in bins of 0.5 mm width (top) and number of particles per bin (bottom) for the simulation run and time instance shown in figure 10 for the three simulated cases with mimicked ion Mach number $M_{th} = 0.0$ (blue lines), $M_{th} = 0.4$ (purple lines), and $M_{th} = 0.7$ (red lines).

quantitatively study self-excited DAWs in any case, we take a common, simpler approach: We model the space charges in the wakes as two positive point charges with a charge of $Q_w = -z \times Q_d$ at distance δ_w up- and downstream from the microparticle. This approach is commonly used to mimic ion wakes in complex plasmas [107–109]. We also modified the simulation routines to not assume reciprocity in the interactions, since this is not given in the case of the wakes.

In order to mimic specific thermal Mach numbers of the ions with the applied point charge model, we plotted the analytic potential (equation (3)) as a function of distance from the central microparticle for the relevant Mach numbers and selected settings for z and δ_w fitting as closely as possible to the analytic potential. We selected $M_{th} = 0.0$: $z = 0.0$, $\delta_w = 16\,\mu$m, $M_{th} = 0.4$: $z = 0.2$, $\delta_w = 10\,\mu$m, and $M_{th} = 0.7$: $z = 0.4$, $\delta_w = 16\,\mu$m.

The simulations were run with timesteps between 10 μs and 0.1 μs, with the lower timesteps for those simulations at higher temperatures. We started with particles on an sq2 lattice (square lattice with two basis atoms, one at the corner and one at the center of the square) with a cell length of $(250-650)\mu$m for the 2D simulations and fcc lattice with cell length $(400-600)\mu$m (before compression by the external confinement). First, we set the gas pressure to 100 Pa (since at low pressures the temperature transfer takes much longer) and then heated the microparticles to break up the lattice. After this, we set the working temperature to a value in the range $(300-10\,000)$ K and allowed the system to relax, and finally set the pressure to the working pressure of 0.38 Pa. This low working pressure is necessary, since without continuous input of energy as in the case of dust acoustic waves, a push with a piston simulated here would be quickly damped at higher pressures.

Then, after some more equilibration at the working pressure, we selected all particles located within a distance of 7.5 mm from the left edge of the simulation box and moved those during a fixed time and velocity into the cloud of particles on the right, basically mimicking the push of a piston. This created a soliton traveling axially through the microparticle cloud. We performed this simulation for several different particle temperatures as controlled with the Langevin thermostat and several different particle number densities. In some simulation runs, the particles were in crystalline state before the push, in others, in the fluid state.

In all cases, the soliton propagated fastest for the simulation run without attractive interaction (mimicking $M_{th} = 0.0$) and slowest for the run with strongest attractive interaction ($M_{th} = 0.7$). In this text, we show results from the 3D run at a microparticle temperature of 1200 K and a lattice length of 400 μm. The average axial particle velocities as a function of axial position are shown in figure B1. These results clearly demonstrate that stronger attraction leads to a slower propagation of waves.

ORCID iDs

M Schwabe https://orcid.org/0000-0001-6565-5890
S A Khrapak https://orcid.org/0000-0002-3393-6767
A M Lipaev https://orcid.org/0000-0002-2559-3696
V I Molotkov https://orcid.org/0000-0001-5809-9312
H M Thomas https://orcid.org/0000-0001-8358-2023

References

[1] Chen T, Zitter R N and Tao R 1992 *Phys. Rev. Lett.* **68** 2555–8
[2] Ashour O, Rogers C A and Kordonsky W 1996 *J. Intell. Mater. Syst. Struct.* **7** 123–30
[3] Dassanayake U, Fraden S and van Blaaderen A 2000 *J. Chem. Phys.* **112** 3851–8
[4] de Vicente J, Klingenberg D J and Hidalgo-Alvarez R 2011 *Soft Matter* **7** 3701
[5] Stanway R, Sproston J L and El-Wahed A K 1996 *Smart Mater. Struct.* **5** 464–82
[6] Liu J, Flores G A and Sheng R 2001 *J. Magn. Magn. Mater.* **225** 209–17
[7] Donado F, Carrillo J L and Mendoza M E 2002 *J. Phys.: Condens. Matter* **14** 2153–7
[8] Szary M L 2002 *Arch. Acoust.* **27** 229–40
[9] Korobko E V and Chernobai I A 1985 *J. Eng. Phys.* **48** 153–7
[10] Wang X Y, Ma N W, Hao-dong W U, Wang H, Hong Y Y, Qin C X and Zhang D 2016 Measurement of acoustic velocity and attenuation of electrorheological fluids *2016 Symp. Piezoelect, Ac. Waves, and Device Appl. (SPAWDA)* (IEEE) p 159
[11] Li L, Wang M, Wang J and Zhao X 2017 *Smart Mater. Struct.* **26** 115006
[12] Nahmad-Molinari Y, Arancibia-Bulnes C A and Ruiz-Suárez J C 1999 *Phys. Rev. Lett.* **82** 727–30
[13] Tiberkevich V, Borisenko I V, Nowik-Boltyk P, Demidov V E, Rinkevich A B, Demokritov S O and Slavin A N 2019 *Sci. Rep.* **9** 9063
[14] Himpel M, Bockwoldt T, Killer C, Menzel K O, Piel A and Melzer A 2014 *Phys. Plasmas* **21** 033703
[15] Merlino R L 2014 *J. Plasma Phys.* **80** 773
[16] Ruhunusiri W D S and Goree J 2014 *Phys. Plasmas* **21** 053702
[17] Jaiswal S *et al* 2018 *Phys. Plasmas* **25** 083705
[18] Du C R *et al* 2012 *New J. Phys.* **14** 073058
[19] Tsai Y Y, Chang M C and I L 2014 *J. Plasma Phys.* **80** 809
[20] Zhdanov S, Schwabe M, Räth C, Thomas H M and Morfill G E 2015 *Europhys. Lett.* **110** 35001
[21] Schwabe M, Zhdanov S and Räth C 2017 *Phys. Rev.* E **95** 041201(R)
[22] Heidemann R, Zhdanov S, Sütterlin K R, Thomas H M and Morfill G E 2011 *Europhys. Lett.* **96** 15001
[23] Fink M A, Zhdanov S K, Schwabe M, Thoma M H, Höfner H, Thomas H M and Morfill G E 2013 *Europhys. Lett.* **102** 45001
[24] Jaiswal S, Schwabe M, Sen A and Bandyopadhyay P 2018 *Phys. Plasmas* **25** 093703
[25] Tsai Y Y, Tsai J Y and I L 2016 *Nat. Phys.* **12** 573–7
[26] Schweigert V A, Schweigert I V, Nosenko V and Goree J 2002 *Phys. Plasmas* **9** 4465–72
[27] Block D, Carstensen J, Ludwig P, Miloch W, Greiner F, Piel A, Bonitz M and Melzer A 2012 *Contrib. Plasma Phys.* **52** 804–12
[28] Jung H, Greiner F, Asnaz O H, Carstensen J and Piel A 2015 *Phys. Plasmas* **22** 053702
[29] Lampe M, Joyce G and Ganguli G 2004 *Phys. Scr.* T **107** 65
[30] Matyash K, Schneider R and Kersten H 2005 *J. Phys.: Conf. Ser.* **11** 248
[31] Lampe M, Joyce G and Ganguli G 2005 *IEEE Trans. Plasma Sci.* **33** 57–69
[32] Kong J, Hyde T W, Matthews L, Qiao K, Zhang Z and Douglass A 2011 *Phys. Rev.* E **84** 016411
[33] Arp O, Goree J and Piel A 2012 *Phys. Rev.* E **85** 046409
[34] Wörner L, Räth C, Nosenko V, Zhdanov S K, Thomas H M, Morfill G E, Schablinski J and Block D 2012 *Europhys. Lett.* **100** 35001
[35] Mitic S, Klumov B A, Khrapak S A and Morfill G E 2013 *Phys. Plasmas* **20** 043701
[36] Melzer A 2014 *Phys. Rev.* E **90** 053103
[37] Rothermel H, Hagl T, Morfill G E, Thoma M H and Thomas H M 2002 *Phys. Rev. Lett.* **89** 175001
[38] Schwabe M, Hou L J, Zhdanov S, Ivlev A V, Thomas H M and Morfill G E 2011 *New J. Phys.* **13** 083034
[39] Schwabe M *et al* 2017 *New J. Phys.* **19** 103019
[40] Schwabe M *et al* 2018 *Microgravity Sci. Technol.* **30** 581–9
[41] Thomas H M, Schwabe M, Pustylnik M, Knapek C A, Molotkov V I, Lipaev A M, Petrov O F, Fortov V E and Khrapak S 2019 *Plasma Phys. Controlled Fusion* **61** 014004
[42] Pustylnik M Y *et al* 2016 *Rev. Sci. Instrum.* **87** 093505
[43] Nefedov A P *et al* 2003 *New J. Phys.* **5** 33
[44] Thomas H M *et al* 2008 *New J. Phys.* **10** 033036
[45] Thoma M H *et al* 2010 *IEEE Trans. Plasma Sci.* **38** 857–60
[46] Sone Y 2000 *Annu. Rev. Fluid Mech.* **32** 779–811
[47] Mitic S, Sütterlin R, Ivlev A V, Höfner H, Thoma M H, Zhdanov S and Morfill G E 2008 *Phys. Rev. Lett.* **101** 235001
[48] Flanagan T M and Goree J 2009 *Phys. Rev.* E **80** 046402
[49] Schwabe M, Rubin-Zuzic M, Zhdanov S, Ivlev A V, Thomas H M and Morfill G E 2009 *Phys. Rev. Lett.* **102** 255005
[50] Schwabe M, Rubin-Zuzic M, Räth C and Pustylnik M 2019 *J. Imaging* **5** 39
[51] Dietz C, Kretschmer M, Steinmüller B and Thoma M H 2017 *Contrib. Plasma Phys.* **58** 21–9
[52] Antonova T, Khrapak S A, Pustylnik M Y, Rubin-Zuzic M, Thomas H M, Lipaev A M, Usachev A D, Molotkov V I and Thoma M H 2019 *Phys. Plasmas* **26** 113703
[53] Khrapak S A *et al* 2005 *Phys. Rev.* E **72** 016406
[54] Khrapak S A *et al* 2012 *Europhys. Lett.* **97** 35001
[55] Khrapak S A, Thoma M H, Chaudhuri M, Morfill G E, Zobnin A V, Usachev A D, Petrov O F and Fortov V E 2013 *Phys. Rev.* E **87** 063109

[56] Ivlev A V *et al* 2008 *Phys. Rev. Lett.* **100** 095003
[57] Ivlev A V *et al* 2010 *IEEE Trans. Plasma Sci.* **38** 733–40
[58] Brandt P C, Ivlev A V and Morfill G E 2010 *J. Chem. Phys.* **132** 234709
[59] Fink M A, Thoma M H and Morfill G E 2011 *Microgravity Sci. Technol.* **23** 169–71
[60] Pustylnik M Y *et al* 2020 *Phys. Rev. Research* in press
[61] Takahashi K and Totsuji H 2019 *IEEE Trans. Plasma Sci.* **47** 4213–8
[62] Melzer A 2001 *Plasma Sources Sci. Technol.* **10** 303–10
[63] Fink M A, Zhdanov S K, Thoma M H, Höfner H and Morfill G E 2012 *Phys. Rev.* E **86** 065401(R)
[64] Takahashi K, Tonouchi M, Adachi S and Totsuji H 2014 *Int. J. Microgravity Sci. Appl.* **31** 18
[65] Barkan A, Merlino R L and D'Angelo N 1995 *Phys. Plasmas* **2** 3563–5
[66] Rosenberg M 1996 *J. Vac. Sci. Technol.* A **14** 631–3
[67] Ratynskaia S *et al* 2004 *Phys. Rev. Lett.* **93** 085001
[68] Schwabe M, Rubin-Zuzic M, Zhdanov S, Thomas H M and Morfill G E 2007 *Phys. Rev. Lett.* **99** 095002
[69] Yaroshenko V V, Khrapak S A, Pustylnik M Y, Thomas H M, Jaiswal S, Lipaev A M, Usachev A D, Petrov O F and Fortov V E 2019 *Phys. Plasmas* **26** 053702
[70] Epstein P 1924 *Phys. Rev.* **23** 710–33
[71] Rao N, Shukla P and Yu M 1990 *Planet. Space Sci.* **38** 543–6
[72] Merlino R L, Heinrich J R, Hyun S H and Meyer J K 2012 *Phys. Plasmas* **19** 057301
[73] Khrapak S A and Yaroshenko V V 2003 *Phys. Plasmas* **10** 4616–21
[74] Khrapak S and Yaroshenko V 2020 *Plasma Phys. Control. Fusion* (https://doi.org/10.1088/1361-6587/aba7f8)
[75] Khrapak S A and Thomas H M 2015 *Phys. Rev.* E **91** 033110
[76] Khrapak S A 2015 *Plasma Phys. Control. Fusion* **58** 014022
[77] Khrapak S A 2019 *Phys. Plasmas* **26** 103703
[78] Yaroshenko V V 2019 *Phys. Plasmas* **26** 083701
[79] Hartmann P, Donkó Z, Rosenberg M and Kalman G J 2014 *Phys. Rev.* E **89** 043102
[80] Khrapak S A and Khrapak A G 2019 *AIP Adv.* **9** 095008
[81] Frost L S 1956 *Phys. Rev.* **105** 354–6
[82] Schwabe M *et al* 2008 *New J. Phys.* **10** 033037
[83] Räth C, Monetti R, Bauer J, Sidorenko I, Müller D, Matsuura M, Lochmüller E M, Zysset P and Eckstein F 2008 *New J. Phys.* **10** 125010
[84] Polyakov D N, Shumova V V, Vasilyak L M and Fortov V E 2010 *Phys. Scr.* **82** 055501
[85] Zobnin A V *et al* 2016 *J. Phys.: Conf. Ser.* **774** 012174
[86] Usachev A D *et al* 2018 *J. Phys.: Conf. Ser.* **946** 012143
[87] Tian R, Yuan C, Bogdanov D V, Bogdanov E A, Kudrzavtsev A A and Zhou Z 2019 *Plasma Sci. Technol.* **21** 115404
[88] Li S, Bogdanov D V, Kudryavtsev A A, Yuan C and Zhou Z 2020 *IEEE Trans. Plasma Sci.* **48** 375–87
[89] Kretschmer M, Antonova T, Zhdanov S and Thoma M 2016 *IEEE Trans. Plasma Sci.* **44** 458
[90] Zobnin A V, Usachev A D, Petrov O F, Fortov V E, Thoma M H and Fink M A 2018 *Phys. Plasmas* **25** 033702
[91] Feng Y, Goree J and Liu B 2007 *Rev. Sci. Instrum.* **78** 053704
[92] Sütterlin K R *et al* 2010 *IEEE Trans. Plasma Sci.* **38** 861–8
[93] Flanagan T M and Goree J 2011 *Phys. Plasmas* **18** 013705
[94] Sun W *et al* 2018 *Europhys. Lett.* **122** 55001
[95] Lin W, Murillo M S and Feng Y 2020 *Phys. Rev.* E **101** 013203
[96] Rosenberg M 2015 *J. Plasma Phys.* **81** 905810407
[97] Kompaneets R, Morfill G E and Ivlev A V 2016 *Phys. Rev.* E **93** 063201
[98] Pompl R 2000 Quantitative Bildverarbeitung und ihre Anwendung auf melanozytäre Hautveränderungen *PhD Thesis* Technische Universität München http://nbn-resolving.de/urn/resolver.pl?urn:nbn:de:bvb:91-diss2000122116573
[99] Sütterlin R 2010 Physics of complex plasmas: some fundamental problems *PhD Thesis* LMU München https://nbn-resolving.org/urn:nbn:de:bvb:19-121324
[100] Räth C and Morfill G 1997 *J. Opt. Soc. Am.* A **14** 3208
[101] Plimpton S 1995 *J. Comput. Phys.* **117** 1–19
[102] Schwabe M and Graves D B 2013 *Phys. Rev.* E **88** 023101
[103] Schwabe M, Zhdanov S, Räth C, Graves D B, Thomas H M and Morfill G E 2014 *Phys. Rev. Lett.* **112** 115002
[104] Epstein P S 1929 *Z. Physik* A **54** 537–63
[105] Kompaneets R, Konopka U, Ivlev A, Tsytovich V and Morfill G 2007 *Phys. Plasmas* **14** 052108
[106] Kana D 2019 Molekulardynamische Simulation von elektrorheologischen Plasmen *Master's Thesis* Justus-Liebig-Universität Gießen
[107] Röcker T B, Ivlev A V, Kompaneets R and Morfill G E 2012 *Phys. Plasmas* **19** 033708
[108] Laut I, Räth C, Zhdanov S K, Nosenko V, Morfill G and Thomas H 2017 *Phys. Rev. Lett.* **118** 075002
[109] Huang H, Ivlev A V, Nosenko V, Lin Y F and Du C R 2019 *Phys. Plasmas* **26** 013702